Prediction and Demonstration of Periodic Dilation Band Formation in Rate-Dependent Porous Cement

Yunxing Lu[a], Manolis Veveakis[b], Dustin Crandall[c], Andrew P. Bunger[a,d,*]

[a] Department of Civil and Environmental Engineering, University of Pittsburgh, Pittsburgh, PA, United States of America.

[b] School of Civil and Environmental Engineering, Duke University, Durham, NC, United States of America.

[c] National Energy Technology Laboratory, US Department of Energy, Morgantown, WV, United States of America.

[d] Department of Chemical and Petroleum Engineering, University of Pittsburgh, Pittsburgh, PA, United States of America.

Abstract

Periodic dilation bands are shown to occur when cylinder-shaped saturated cement specimens are subjected to rapid decompression, with the spacing between the bands scaling as a power law of the decompression time. This behavior is predicted by theory, which is specified to this scenario based on prior work that was more general and applied to compaction. Specifically, the formation of the bands is shown to coincide with periodicity that naturally arises in the effective stress when the material follows a Terzaghi-type consolidation law, although in reverse for dilation and with material deformation described by a rate-dependent viscoplastic law. When strain rate is proportional to effective stress to a power that is greater than one, periodic regions of tensile effective stress arise through the poromechanical fluid-solid coupling. The theoretically-predicted exponent of the resulting power-law relationship between dilation band spacing and unloading time successfully brackets the experimental results, for which it is observed that the exponent is slightly stronger than a square-root relationship (0.28 to 0.67) at testing temperatures of 20 °C and 90 °C. These results demonstrate that rapid-depressurization leads to periodic fracturing that could, on the one hand, be detrimental to the isolation provided by cement used to seal wellbores in the petroleum industry. On the other hand, the dilation bands could also be favorable to production if generated in low-permeability reservoir rocks such as shales that are targeted for petroleum production or granites that are targeted for geothermal energy.

1. Introduction

Deformation bands that occur in porous geo-materials comprise one important line of evidence for the stress history of the rock. They are mainly categorized into three types of tabular geological structures: shear bands, compaction bands and dilation bands (R. I. Borja, 2004; Du Bernard et al., 2002; Eichhubl et al., 2010; Fossen et al., 2007; Gapais, 1989; Issen & Rudnicki, 2000; Wolf et al., 2003). Many of these deformation bands in natural rocks are low-displacement deformation zones of millimeters to centimeters thickness that tend to have different cohesion and permeability compared with ordinary fractures (Fossen et al., 2007). The observable features of these deformation bands can reveal information about the local glacial history, the generation process of soft-sediment deformation or post-burial faulting. They can also significantly alter fluid flow patterns by their impact on the permeability of the geo-materials, in some cases by several orders of magnitude (Antonellini & Aydin, 1994, 1995; Fossen et al., 2007; Jamison & Stearns, 1982; Pittman, 1981). As one example, Sigda et al. (1999) found that the deformation bands that occur in the low porosity formations can induce flow channeling which can determine pathways for groundwater flow through the vadose zone. This channelization phenomenon can also be observed during the production of a petroleum reservoir where deformation bands may be forming in low-permeability reservoir rocks during the stimulation phase of reservoir development (Fossen et al., 2007).

Given the distinctive characteristics of the deformation bands and information they can provide for geoscientists and engineers, considerable attention has been devoted to understanding the conditions and mechanisms that control their formation. It has been previously concluded that factors such as porosity, mineralogy, and grain size and shape will have some influence on the deformation band formations, but they are mainly controlled by three main factors (Fossen et al., 2007; W. A. Olsson, 1999; Rudnicki & Rice, 1975). These are: 1) geometry (kinematic boundary conditions, layering, etc.), 2) the constitutive response of the material (viscous, elastic, viscoelastic, etc.), and 3) the under-pinning multi-physical coupling and competitions processes.

Band width and spacing, which is one of the most readily observable of their features, are a focal point of many studies including recent reviews (Jacquey et al., 2021; Regenauer-Lieb et al., 2013). Based on the classical constitutive modeling approach from elasticity and plasticity, and combining the multi-physical coupling processes with their respective length and time, an

overarching feature is the explicit emergence, at various scales, of deformation bands as dissipative patterns from the behavior of the energy equations. The body of previous literature also provides a sound basis to incorporate multiple physical principles such as coupling the laws of thermodynamics, material balances, and constitutive models and, as one might expect, each physical principle brings characteristic length and/or time scales thereby leading to different length and time scales associated with the predicted emergence of deformation bands.

One research area focuses on deformation bands associated with fundamentally slow processes, for example examining formations of these patterns in response to tectonic strain rates in the range of 10^{-12} to 10^{-16} s^{-1} (Jackson & Talbot, 1986; Pfiffner & Ramsay, 1982). However, at the other end of the spectrum in terms of characteristic time scales, deformation bands could also be induced in low-permeability porous geo-materials such as shale and cement from engineering processes which involve rapid pressurization/depressurization. Such rapid processes can come at the beginning of a well's life, for example, from pressure fluctuations induced by reservoir stimulation (i.e. hydraulic fracturing). They can also come at the end of a well's life, for example from the rapid depressurization required as a part of a canonical cement plug test that is often required in order to verify integrity as a part of permanent plugging and abandoning of wells (Khalifeh & Saasen, 2020). Because they involve changes in stresses and/or fluid pressures that are of a similar order to the strength of the rock (order of tens of MPa) over timeframes where pore pressure often cannot drain (seconds to tens of minutes), these engineering processes have potential to induce failure of geomaterials due to coupled poromechanical processes (see e.g. Detournay and Atkinson (2000); Lu and Bunger ; Pearson (1981); Schmitt and Zoback (1989)).

With there being a possibility of cement and rock to fail as a result of rapid engineering processes, the tendency of failing geomaterials to form periodic deformation structures is important to understand if such material failure is to be either avoided (i.e. for cement integrity) or pursued (i.e. for reservoir stimulation). Past investigations mainly focus on compaction and shear bands (Baud et al., 2004; Bésuelle, 2001; Okubo & Schultz, 2005; W. Olsson & Holcomb, 2000; W. A. Olsson, 1999; W. A. Olsson et al., 2004; Wong et al., 2001). As for dilation bands, they have been previously observed in highly porous media (Du Bernard et al., 2002). However, little (possibly no) experimental evidence of the formation of dilation bands in low-permeability materials has been observed and reported in the literature. As a consequence, the underlying

mechanisms responsible for the formation of dilation bands have not been fully discussed or definitively characterized. The formation of dilation bands may encompass substantial grain rotations and translations, a process bearing resemblance to the formation of compaction and shear bands. Nevertheless, Fossen et al. (2007) have emphasized that tension fractures, stylolites, and/or slip surfaces are more inclined to emerge during the development of dilation bands, particularly in media with very low permeability. Even so, the mechanism(s) of the formation of dilation bands is still a knowledge gap that is addressed here by showing that dilation bands occur in experiments performed in the laboratory on low-permeability, low-porosity cement when it is subjected to rapid reduction in applied stress (decompression). After reviewing a recent theoretical framework for compaction band spacing predictions, this paper extends this theory to the dilation bands family and presents a series of experimental demonstrations. Furthermore, discussions of the implications for practice, especially the methods used for cement plug verification which could damage the integrity they are intended to ensure are also included.

2. Governing Equations of Periodic Dilation Band Theory

A theoretical framework for prediction of deformation bands was recently developed by (E Veveakis & Regenauer-Lieb, 2015) and Jacquey et al. (2021). The prior work is more general at first and then is specified to a form that describes compaction bands under 1D strain conditions. An alternate derivation and summary that is instead targeted to the present interest of dilation bands begin with a simplified one dimensional (1D) problem formulation under the assumption of homogenous deformation where the orientation of the coordinate system (denoted with coordinate z) is selected according to the approach of Issen and Rudnicki (2000) so as to be orthogonal to the anticipated orientation of compaction/dilation bands. Expressing stress equilibrium in the z direction for a material with no body force and under static conditions, as well as stating the definition of Terzaghi's effective stress, gives

$$\frac{d\sigma_{zz}}{dz} = 0\,, \tag{1}$$

$$\sigma_{zz}^{'} = \sigma_{zz} - p\,. \tag{2}$$

Here σ_{zz} is the normal total stress acting in the z direction, $\sigma_{zz}^{'}$ is Terzaghi's effective stress (the part of the total stress that is bearing on the solid matrix), and *p* is the pore pressure. Combining these leads to

$$\frac{\partial \sigma_{zz}^{'}}{\partial z} = -\frac{\partial p}{\partial z}, \tag{3}$$

Note that compressive stresses are taken to be positive in this sign convention.

Next one needs to express mass balances. This begins for a saturated porous medium by defining the partial densities of solid skeleton phase (ρ_s) and fluid phase (ρ_f). These are defined as mass of skeleton and mass of fluid over the volume of porous material, respectively. These relate to the density of each constituent (i.e. the mass of solid over volume of solid and mass of fluid over volume of fluid) via porosity *n*, via

$$\rho_s = (1-n)\rho_1, \tag{4}$$

$$\rho_f = n\rho_2. \tag{5}$$

Here we denote the constituent densities as $\rho_i (i = 1,2)$, where 1 represents the solid skeleton and 2 represents the fluid. Then in the general case where local mass exchange between the matrix and the voids (i.e. pores) is allowed, the mass balance equations for the solid and fluid phases are (E Veveakis & Regenauer-Lieb, 2015)

$$\frac{1-n}{\rho_s}\frac{\partial \rho_s}{\partial t} - \frac{\partial n}{\partial t} - \frac{\partial n v_z^s}{\partial x_z} + \frac{\partial v_z^s}{\partial x_z} = 0, \tag{6}$$

$$\frac{n}{\rho_f}\frac{\partial \rho_f}{\partial t} + \frac{\partial n}{\partial t} + \frac{\partial n v_z^f}{\partial x_z} = 0, \tag{7}$$

In these expressions, v_z^s and v_z^f are the partial velocities of the solid and fluid in the *z*-direction, respectively. Furthermore, if the solid and fluid phases are both considered as incompressible, i.e., if ρ_s and ρ_f are constant and do not change with time (leading to a time derivative of zero), Eq.6 and Eq. 7 reduce to

$$-\frac{\partial n}{\partial t}-\frac{\partial n v_z^s}{\partial z}+\frac{\partial v_z^s}{\partial z}=0\,, \tag{8}$$

$$\frac{\partial n}{\partial t}+\frac{\partial n v_z^f}{\partial z}=0\,. \tag{9}$$

By summing Eq.8 and Eq.9, the mass balance equation of the mixture is obtained as

$$\frac{\partial n(v_z^s-v_z^f)}{\partial z}+\frac{\partial v_z^s}{\partial z}=0\,. \tag{10}$$

Next we introduce the classical expression of the Gersevanov filter velocity $n(v_z^f-v_z^s)$ given by (Gersevanov, 1937)

$$n(v_z^f-v_z^s)=-\frac{k_\pi}{\mu_f}\frac{\partial p}{\partial z}+\rho g+h.o.t.\,, \tag{11}$$

where g is gravitational acceleration, μ_f the viscosity of the fluid ($Pa\,s$), and k_π permeability (m^2), which is assumed as constant in this study as commonly done in consolidation theory. Additionally, the higher order terms (h.o.t.) refer to the nonlinear models of the flux. By neglecting the higher order terms as well as the gravitationally-driven part of the flux, the Gersevanov velocity reduces to an expression of Darcy's law, that is

$$n(v_z^f-v_z^s)=-\frac{k_\pi}{\mu_f}\frac{\partial p}{\partial z}\,. \tag{12}$$

This expression of Darcy's law will be substituted to the first expression in Eq. (10). To address the second expression in Eq. (10), we recognize that it is giving rate of the normal infinitesimal strain rate in the z-direction ($\dot{\varepsilon}_{zz}$), that is

$$\dot{\varepsilon}_{zz}=-\frac{\partial v_z^s}{\partial z}\ , \tag{13}$$

Here the minus sign is from the compression-positive sign convention. The strain rate can be decomposed into elastic and plastic parts

$$\dot{\varepsilon}_{zz}=\dot{\varepsilon}_{zz}^{(e)}+\dot{\varepsilon}_{zz}^{(p)}\,. \tag{14}$$

If some linear relationship between the elastic strain rate and the effective stress is assumed (as in classical consolidation theory), then

$$\dot{\varepsilon}_{zz}^{(e)} = a\dot{\sigma}_{zz}^{'}, \tag{15}$$

where a is the compressibility. Furthermore, consider the plastic deformation to be described via a rate-dependent viscoplastic power law of the well-studied form (R. Borja & Kavazanjian, 1985; Hickman & Gutierrez, 2007; Taylor, 1948)

$$\dot{\varepsilon}_{zz}^{(p)} = sgn(\sigma_{zz}^{'})\eta\left[\frac{\left|\sigma_{zz}^{'}\right|}{\sigma_{ref}}\right]^{m}, \tag{16}$$

where η is the creep parameter (in s^{-1}), m is the material sensitivity (R. Borja & Kavazanjian, 1985; Hickman & Gutierrez, 2007), and σ_{ref} a reference stress which depends on the loading condition used to obtain the creep parameter and material sensitivity. The value selection of these parameters for this problem will be discussed later. For now, by substitution of Eq. (3), (13), (14), (15) and (16) into Eq. (12), one can obtain the diffusion equation that considers both elastic and plastic strain

$$\frac{\partial^2 S^{'}}{\partial \xi^2} = \frac{a\mu_f L^2}{k_\pi}\frac{\partial S^{'}}{\partial t} + sgn(S^{'})\frac{\eta\mu_f L^2}{k_\pi \sigma_{ref}} S^{'m}, \tag{17}$$

where $S^{'} = \frac{\sigma_{zz}^{'}}{\sigma_{ref}}$ and $\xi = \frac{z}{L}$. This governing equation for the effective stress can be solved provided with appropriate initial and boundary conditions along with the necessary inputs of material properties. Behavior of the solution for cases relevant to the depressurization of a cylinder is described in the next section.

4. Behavior of the Model

This section presents a range of solution behaviors of the governing equations. Ideally, the material sensitivity m will be determined from either a creep or relaxation test under the relevant testing conditions, with each test potentially take up to a week or even more. Unfortunately, due to constraints and limitations on the available experimental equipment, the material sensitivity m can not be experimentally determined directly. Thus, some simplifications and specifications will be made firstly before discussing how the value selections of the material sensitivity m will influence on the solutions of the model.

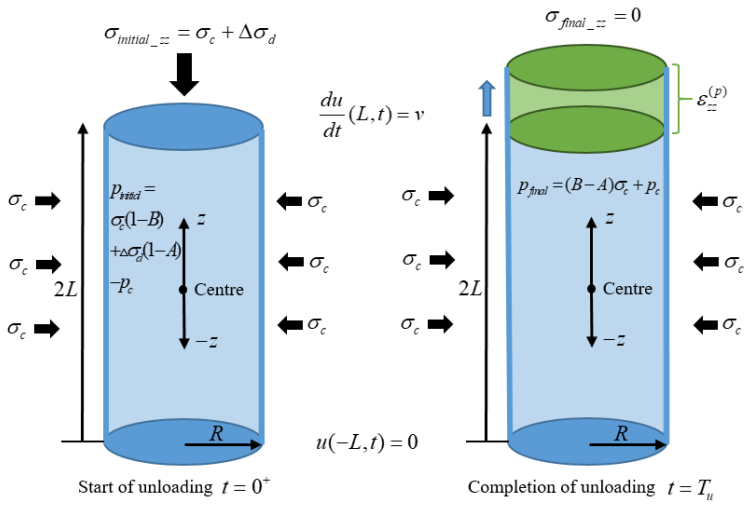

Figure 1. Illustrations of the initial and boundary conditions during dilation in the unloading progress.

Figure 1 shows a 1D cylindrical sample that is used for a convenient geometry that illustrates how the unloading can progress to generate the dilation bands. During such axial decompression under the undrained conditions, the plastic part of the strain ($\varepsilon_{zz}^{(p)}$) is considered as the primarily contributor to the local fluctuations and pore fluid flow. It is also considered large in magnitude in comparison to the elastic part of the strain ($\varepsilon_{zz}^{(e)}$). This perspective is consistent with the consolidation theory which emphasizes the processes that most significantly affect the capacity for fluid storage, namely the changes in porosity. If the majority of porosity alterations are viscoplastic in nature, the system manifests complex behaviors that constitute the focus of this study. So, with this assumption, the immediate response part of the Eq. (17) is dropped here with the idea that the elastic strain will generate very little change in porosity, so that Eq. (17) becomes

$$\frac{\partial^2 S'}{\partial \xi^2} = sgn(S')\frac{\eta \mu_f L^2}{k_\pi \sigma_{ref}} S'^m . \tag{18}$$

Now we turn our attention to the initial conditions relevant to the problem of axial decompression. Consider the experimental procedures that include a gradual elevation to the hydrostatic state, then a slow increase in deviatoric stress to the targeted value. Following these steps, the entire system is allowed to stabilize for an additional 20 minutes under these conditions before initiating the decompression process. Hence, before considering the decompression problem, we need to consider the loading stage. In this stage, the sample is loaded by a confining

stress σ_c and deviatoric stress $\Delta\sigma_d$. This loading (taken as an increase in the total stress) will be partitioned between a part that is carried by the pore fluid and a part that is carried by the solid skeleton, where the former is the pore pressure and the latter is the effective stress (recall Eq. (2) (Biot, 1941; Terzaghi, 1925). Furthermore, after the immediate response of the pore pressure, there is a possibility of additional transfer of the total stress from the skeleton to the pore fluid as the skeleton undergoes some permanent deformation. As reported by Wyrzykowski et al. (2019) and Tamtsia et al. (2000), a significant portion of creep deformation actually occurs at the very early stage of creep, almost immediately following the application of deviatoric loading. It is therefor assumed that a considerable amount of plastic deformation already occurs during the stabilization time, leading to the induction of creep pore pressure. With these considerations, after applying and holding the initial loading, the resulting pore pressure is

$$p_{load} = B\sigma_c + A\sigma_d + p_c, \tag{19}$$

where A is Biot's coefficient of effective stress, B is Skempton's pore pressure coefficient and p_c is creep-induced pore pressure. The poromechanics-related parameters A and B have been extensively studied by Detournay and Cheng (1988) and Cheng (1993) and their value ranges have been reported in the literature (Agofack et al., 2019; Ghabezloo, 2010; Ghabezloo et al., 2008). It is also worth noting that Detournay and Cheng (1988) also provide an explicit form for Biot's coefficient of effective stress as a function of Skempton's pore pressure coefficient, with the Poisson's ratio depending both on drained and undrained conditions. So, after applying the initial loading, the total stress is

$$\sigma_{load\_zz} = \sigma_c + \Delta\sigma_d, \tag{20}$$

The initial dimensionless effective stress can thus be expressed as

$$S'(\xi,0) = \frac{\sigma_{load\_zz} - p_{load}}{\sigma_{ref}} = \frac{\sigma_c(1-B) + \sigma_d(1-A) - p_c}{\sigma_{ref}}. \tag{21}$$

During the subsequent unloading (decompression) period, which consists of moving the top platen at a constant velocity for a travel distance (u) until the entire axial stress is zero after the total unloading time T_u, the boundary conditions are maintained as

$$u(-L,t)=0\,,\ \frac{du}{dt}(L,t)=v_z\,, \tag{22}$$

and the resulting plastic strain rate can be defined as

$$\dot{\varepsilon}_{zz}^{(p)}=\frac{\varepsilon_{zz}^{(p)}}{T_u}\,. \tag{23}$$

When the unloading is completed, the total stress in the z-direction returns to zero ($\sigma_{final\_zz}=0$) and, assuming sufficiently rapid unloading so that undrained conditions apply, the pore pressure (p_{final}) at this moment is

$$p_{unload}=(B-A)\sigma_c+p_c\,. \tag{24}$$

Thus, at the end of unloading, the effective stress is

$$\sigma'_{unload\_zz}=\sigma_{unload\_zz}-p_{unload}=-((B-A)\sigma_c-p_c)\,. \tag{25}$$

During this decompression process, the creep parameter η and the reference stress σ_{ref} can take the value of $\dot{\varepsilon}_{zz}^{(p)}$ and $\sigma_{ref}=(B-A)\sigma_c-p_c$, respectively, as Veveakis et al. (2015) show that these value selections are valid in the compaction band framework. In the dilation process, the effective stress boundary condition in the dimensionless form is

$$S'(-1)=S'(1)=\frac{\sigma'_{unload\_zz}}{\sigma_{ref}}=-1\,. \tag{26}$$

Following sign conventions mentioned above, the negative sign indicates that the effective stress is tensile which in turn results in $-sgn(S')=-1$. Then, the Eq. (18) becomes

$$\frac{\partial^2 S'}{\partial\xi^2}+\zeta S'^m=0\,, \tag{27}$$

where ζ is a dimensionless unloading rate given by

$$\zeta=\frac{\varepsilon_{zz}^{(p)}}{T_u}\frac{\mu_f L^2}{k_\pi[(B-A)\sigma_c+p_c]}\,. \tag{28}$$

The solutions of Eq. (27) are dependent on material sensitivity m. For all $m>1$, the solution has singularities (Emmanuil Veveakis et al., 2010). The solution, in general, requires numerical

methods. However, closed-form analytical solutions exist for m=2 and m=3 (after Regenauer-Lieb et al., 2013). The m=2 solution has some desirable features (namely, the effective stress is symmetric rather than antisymmetric about the singularities), and so we focus on the m=2 solution which is expressed as

$$S' = \frac{6}{\zeta}\wp(\xi + c_1, 0, c_2), \text{ when } m = 2; \tag{29}$$

where $\wp(u, \omega_1, \omega_2)$ is the Weierstrass P function (Abramowitz & Stegun, 1964). Taking the coefficient $c_1 = 0$ ensures the symmetrical distributions of S' about the center ($\xi = 0$) of the specimen along the ξ direction. With this symmetry, the boundary conditions from Eq. (26) can both be satisfied by appropriate selection of c_2, which is the solution of a transcendental equation obtained by expression Eq. (29) at $\xi = \pm 1$. The value of c_2 is therefore dependent on the ζ value, and so must be solved numerically for each given value of ζ. The result is a family of solutions that depend on ζ, as shown in Figure 2. Clearly the solution is characterized by periodic singularities, which generate periodically-distributed regions of tensile effective stress and therefore have the potential to generate periodic tensile fracturing, i.e. “dilation bands”.

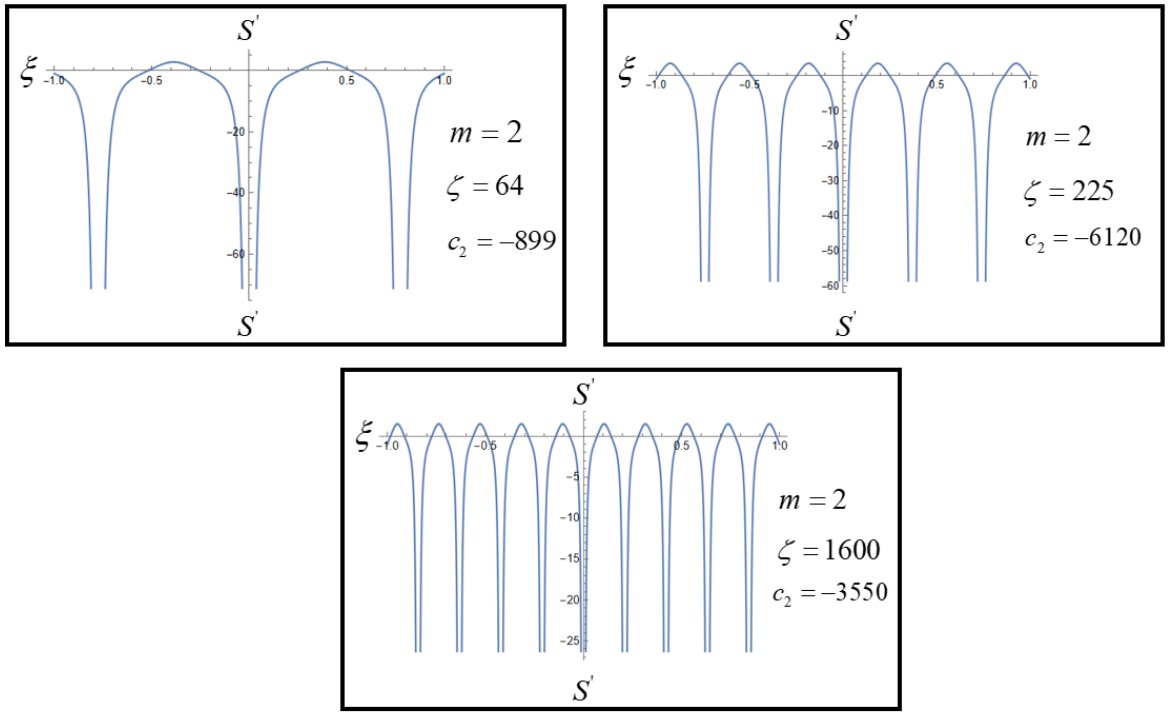

Figure 2. Different solution behaviors of S' when material sensitivity $m = 2$ and ζ is taking different values.

In the Discussion section that is to follow, we will reflect on the physical nature of the coupling that leads to periodic regions of tensile effective stress. At this point, we will focus on the dependence of the period of the tensile stress regions on ζ with the anticipation that we can vary this quantity in the laboratory by varying the unloading rate and in this sense test the utility of the model for predicting dependence of the dilation band spacing on unloading rate. To this point, when $m = 2$, the number of singularities (N) on the domain $-1 \le \xi \le 1$ is scaling as a power law of ζ, with the exponent of the power law taking on different values depending upon the range of ζ (Figure 3). Hence, we describe the number of singularities as

$$N = \lambda \zeta^{\gamma} \tag{30}$$

Based on Figure 3, when ζ is in the range from ~20 to ~200, the number of singularities (N) is scaling with ζ at an exponent of 0.67. However, when ζ ranges from ~200 to ~1600, the number of singularities (N) is scaling with ζ at a smaller exponent of 0.28. Between distinctive power laws lies the region of $100 \le \zeta \le 1000$, which is of interest because it is where the number of singularities is between 2 and 7. Hence it is a region where the number could be readily observed in experiments. In this region, the behavior will not strictly follow a power law, however, if one were to fit a power law the exponent would be expected to be around ½, as illustrated by the orange color sketched line with a slope of $N \propto \zeta^{1/2}$.

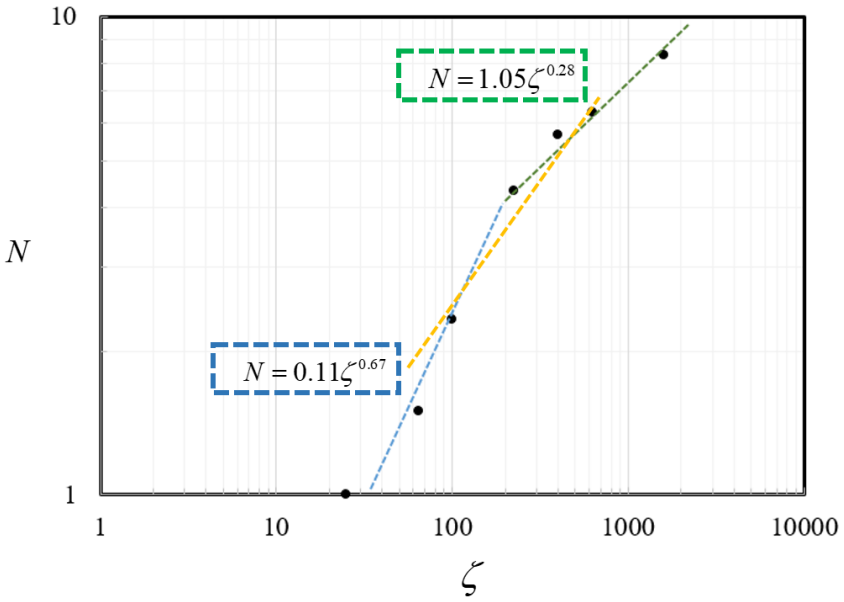

Figure 3. When $m = 2$, two different power law relationships occur between the number of singularities (N) and ζ based on different ranges of ζ. The orange dash line is an illustration for fitting purpose when the exponent is 1/2.

4. Experimental Demonstration

4.1 Experimental Setup and Procedures

The decompression tests are performed in a temperature-controlled Hoek-type triaxial cell. This system consists of three main parts: axial loading system, confining stress system, and temperature-control system (Figure 4). The deviatoric loading is controlled by an INSTRON-600DX load frame, which can provide up to 600KN. The confining stress is maintained by a high-pressure syringe pump (ISCO-260D), which is also allowing precise measurement of the volume change of the specimen associated with a given confining stress up to 70 MPa. The temperature is provided by wrapping the Hoek cell with the heating tape that can provide a controlled temperature up to 180°C. The material used in the experiments is Portland cement paste without any aggregate. The selection of this material was based on its accessibility and the simplicity of casting and its relevance to the application area of wellbore integrity, owing to the fact that such cement-only materials types are used to provide the seal between the casing and rock formation in many types of wells. From the perspective of the mechanical study, it is important to realize that although the hardened cement paste is usually considered as a quasi-brittle material, it exhibits significant time-

dependent behaviors, including creep, which has been reported by Tamtsia and Beaudoin (2000) and Wyrzykowski et al. (2019). According to their research, the material exhibits viscoplasticity, a characteristic derived from the intricate hydro-chemical-thermal coupling processes within the C-S-H of the cement matrix. Furthermore, they found that a considerable part of the viscoplastic deformation takes place at the initial stages of creep, practically instantaneously following the application of deviatoric loading. At the same time, the cement paste is considered to have relatively low tensile strength (2 to 5 MPa) when compared to concrete (Katende et al., 2020; Li & Li, 2015). Therefore, this material aligns well with one of objectives of this study, specifically, to explore formation of dilation bands in decompression laboratory experiments.

In the experimental procedure for performing the decompression tests, the cylindrical specimen (60 mm height; 30 mm diameter) is kept at 100% water moisture content conditions (submerged in water) after demolding. Then it is further subjected vacuum saturation at a pressure of -1 bar for a period of 48 hours before the test. After saturation, the specimen is placed into the membrane, which is specially designed to attach to the cell so that the whole system remains airtight (Figure 5). After the membrane with a specimen inside is placed into the Hoek cell, hydraulic oil is pumped into the space between membrane and cell so the lateral pressure can be provided. The specimen is axially enclosed by two steel loading plates (top-loading plate and bottom spacer). The top vertical piston of the load frame directly contacts the top-loading plate so the deviatoric load can be applied. By using heating tape wrapped around the Hoek cell, the temperature of the cell is slowly increased to the targeted temperature, i.e., 90°C, over two to three hours while maintaining a low hydrostatic (both confining and axial) applied stress of 1.4 MPa. Note that by requiring hours for the heating process, it is possible to drive some evaporation of pore fluid so that the specimen can potentially deviate from fully saturated conditions. However, a slow heating phase is required to avoid the pressurization of the pore fluid due to fast thermal loading. The airtight seal between membrane and specimen and the tight contact between the steel platens and the ends of the specimen is relied upon to prevent evaporation, which is one motivation to perform the heating under a hydrostatic applied stress.

After the desired system temperature is achieved and stabilized, the confining pressure and vertical load are increased to the targeted pressure value of 13.7 MPa, so the specimen is initially

366 loaded isotropically. Next, the deviatoric load is increased to the targeted value of 20.7 MPa and
367 held for a short period of time (around 15 minutes) to make sure the system is stabilized.

368 After this holding period (akin to the initial loading described in the previous section), the
369 the axial stress is released by prescribing a set rate of motion of the actuator that is responsible for
370 applying the axial load. During this time, the axial load is completely released, and the radial load
371 is still maintained at the value of the confining stress. The hydraulic properities of such cement
372 pastes have been extensively studied from the lieterature (Banthia & Mindess, 1989; Goto & Roy,
373 1981; Nyame & Illston, 1981). Considering the reported permeability range of (1e-15 – 1e-18 m^2),
374 the diffusion time could span from a few days to several months. In contrast, both the loading time
375 and the slowest unloading time, at around 30 seconds, are very brief in comparison to the diffusion
376 time. Consequently, the transient diffusion process is disregarded in the interpretation of these
377 experiments; the material is effectively undrained.

378 This comprises the experiment as far as the mechanisms of interest are concerned. Hence,
379 the final unloading of the radial stress is done very slowly, after which the specimen is removed
380 for inspection and measurement. These are done both visually and by scanning by a North Star
381 Imaging M-5000 Computed Tomography (CT) scanner with Feinfocus FXE source at 185 kV and
382 200 mA.

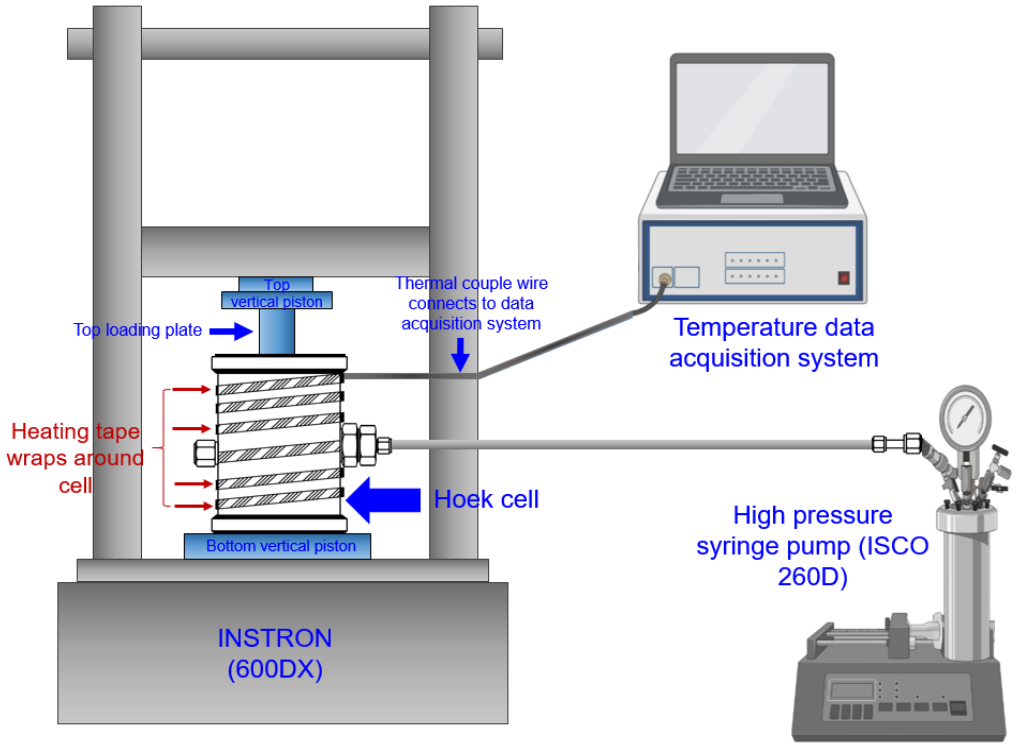

Figure 4. Experimental setup of the decompression tests, includes the axial loading system, confining stress system, and temperature-control system.

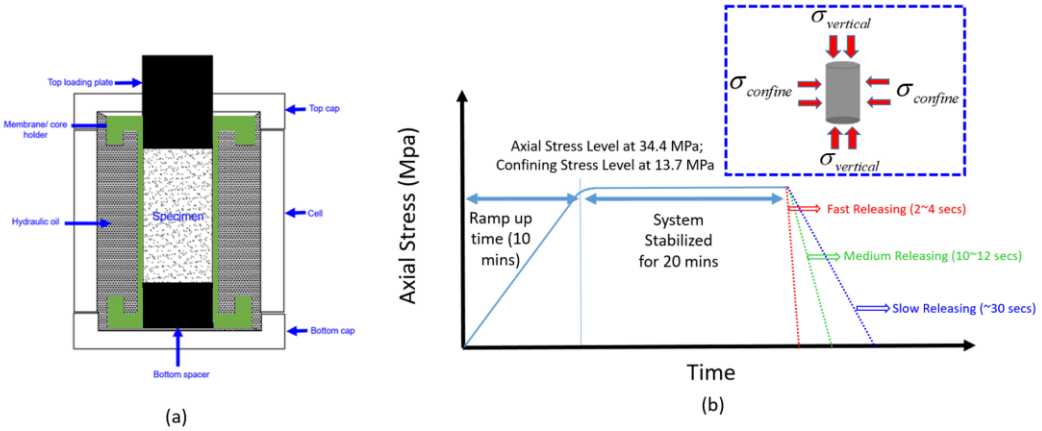

Figure 5. (a) The internal structure of the Hoek-cell; (b) Specimen with its boundary conditions and the loading and unloading paths.

4.2 Experimental Results

The observed fractures (the locations are indicated as green arrows) and their spacing from the experiment are shown in Figure 6. Note that there are two types of fractures that are observed.

Taking the fast release at room temperature (top left corner) as an example, fractures (f1, f2, and f3) are penetrating-through fractures which are completely separating the whole cross section of the sample. These fractures can be observed by visual inspection. However, the internal fractures (f4 and f5) are not visible by inspection of the outer surfaces of the specimen, but they are visible in the CT scans. The spacing between these experimental observed fractures and the corresponding unloading time to generate these fractures are summarized in Table 1.

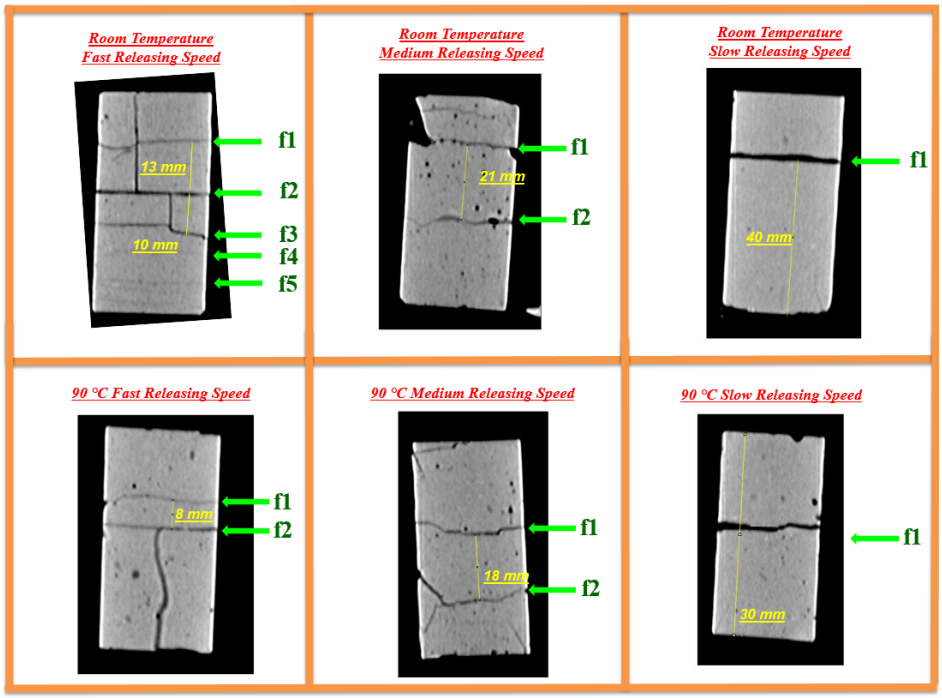

Figure 6. Measurement of tensile bands spacing occurs during decompression test at room temperature and 90 ℃. The location of each observed fractures is indicated and labeled by an arrow on the right side.

Table 1. Unloading time and experimental measured spacing of each specimen in Figure 7

Testing Temperature	Unloading Time (s)	Experimental Measured Spacing (mm)
Room Temperature	3 (fast)	11.5
Room Temperature	11 (medium)	21
Room Temperature	30 (slow)	40
90°C	3 (fast)	8
90°C	11 (medium)	18
90°C	30 (slow)	30

4. Discussion

Knowing the sample length ($2L$) and the predicted number of singularities, a relationship for the spacing between singularities (fractures) h and the unloading time (T_U) is obtained as

$$h = \frac{2L}{N} = \frac{2L}{\lambda}\left[\frac{\varepsilon_{zz}^{(p)}}{T_u}\frac{\mu L^2}{k_\pi[(B-A)\sigma_c + p_c]}\right]^{-\gamma} \propto T_u^{\gamma}. \quad (31)$$

As discussed in the last section, the exponent γ is dependent on the parameters of m and ζ. Its range is from 0.28 to 0.67 when m=2. As shown in Figure 7, the power law relationship between the experimental observed spacing and the unloading time is plotted in log-log space, the exponent at high temperature (90℃) is found as 0.5764 with R^2 = 0.9968 and the exponent at room temperature (20℃) is found as 0.5376 with R^2=0.9913. These reported values are falling into the reasonable ranges of exponents when m=2. This is especially true when considering that the total number of observed dilation bands is consistent with ζ being in the range of 100 to 1000. For m=2, if one had only three of the model predictions across this limited range, inspection of Figure 2 shows that the apparent exponent of a power law would be near 0.5. Hence, these experimental results give support to the scaling relationships between the numbers of tensile effective stress regions and ζ based on the theoretical framework of periodic dilation band formation in rate-dependent porous materials.

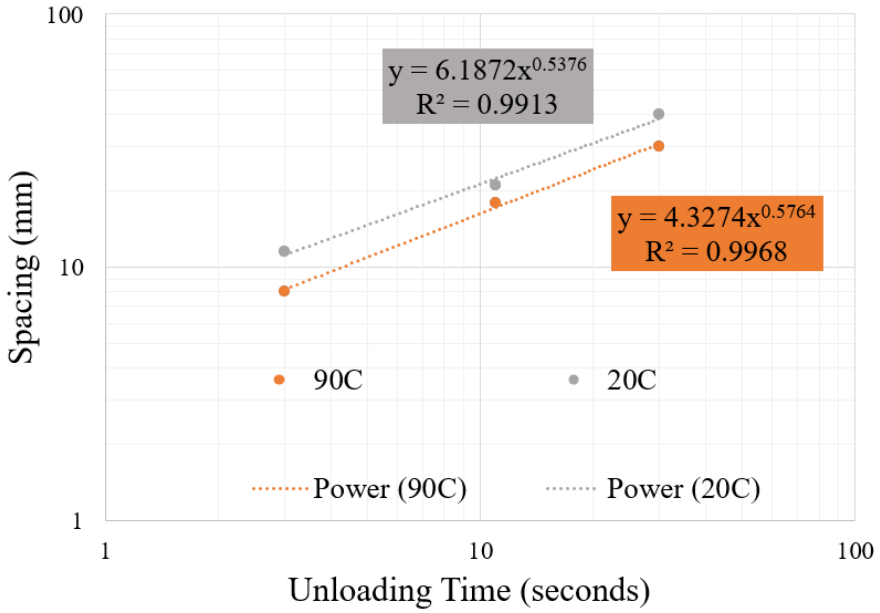

Figure 7. Power law relationship between unloading time and spacing from the experimental observation is summarized in Table 1.

Post-experiment inspection of the fracture surfaces shows no evidence of crushing, pore collapse, or sliding. Hence it is consistent with a tensile mechanism and stands in contrast with prior work on deformation bands observing different modes that show evidence of grain translation, shear displacement, or even crushing in poorly consolidated sand and sandstone (Du Bernard et al., 2002). It is therefore worth reflecting on the coupled mechanisms that lead to the formation of these dilation bands (DBs).

Beginning from the moment the axial load begins to be removed from the specimen, the internal coupling becomes complex as the movement of the fluid (following diffusion law) and movement of the solid (viscoplastic law) interplay. Because the starting point is the conservation of both solid and fluid phases, the movement of these phases must be counter to one another. That is, as the solid deforms and thus moves in a certain direction (dilation direction), mass balance requires there to be a counterflow of fluid. So, if we examine what happens in the moments leading up to the sample being completely unloaded in the axial direction, there is a dilation process relative to the loaded state. Because of the pore pressure generated during the loading that is then unable to be dissipated on the rapid timescale of the unloading, the effective stress becomes

443 negative (tensile) everywhere. By the viscoplastic law, the volumetric strain rate has the same sign
444 as the effective stress, which means the sample is volumetrically dilating.

445 If this dilation is initially uniform, consider what would happen if there is a small
446 perturbation locally within the specimen to become even smaller (more tensile). By the
447 viscoplastic law, the dilational strain rate will become even greater at that location. This dilational
448 strain amounts to a movement of the solid phase away from the location of the perturbation. But,
449 throughout this process, the total stress must remain constant in order to satisfy equilibrium, which
450 means that the reduction of the solid phase at that location will transfer more of the load to the
451 fluid phase. This will elevate the pore pressure at the location of the perturbation, thus leading the
452 effective stress to become even more negative. This leads to a further acceleration of the local
453 strain (dilation) and an additional transfer of load to the pore fluid, raising the pore pressure and
454 thus further decreasing effective stress in order to maintain constant total stress. In this way, a local
455 perturbation can grow unstably unless it is somehow mitigated by the rate at which fluid pressure
456 can equilibrate between the local perturbation with high pore pressure and the "far-field" relative
457 to the perturbation with low pore pressure. In this regard, the dilation bands can be seen as a form
458 of material instability existing in a coupled poromechanical system, eventually leading to a
459 separation of the solid phase into a dilation band (as illustrated in Figure 8).

460 With this in mind, the solution to the coupled governing equations is therefore indicating
461 the natural spacing that is predicted to arise as some perturbations grow and others are suppressed,
462 with growth and suppression representing a competition between the rate of solid deformation and
463 the rate at which diffusion can dissipate accumulating pore pressure. This competition is indeed
464 embodied in the form of the dimensionless strain rate, ζ, which is directly proportional to the solid
465 strain rate and inversely proportional to the fluid diffusivity (permeability over fluid viscosity).
466 When this ratio is small (higher diffusivity and/or lower strain rate), the fluid diffusion can take
467 place at a larger scale and so the spacing between tensile regions is larger. When this ratio is higher
468 (smaller diffusivity and/or higher strain rate), fluid diffusion can only occur at a smaller scale and
469 so the spacing between tensile regions resulting from this coupled process becomes smaller.

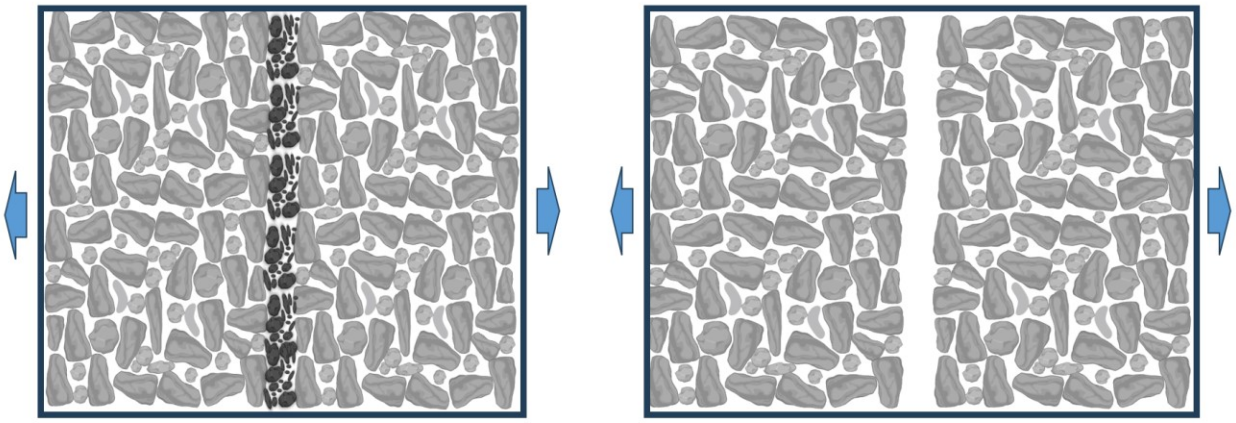

Figure 8. Left: Compaction band surface is characterized by grain translation, displacement, or even crushing in poorly consolidated sand and sandstone; Right: dilation band surface is characterized by planar opening-mode fractures with two discrete and neat surfaces in the low permeable porous materials.

The previously-reported compaction bands are proposed to work in the opposite way. During the compaction process, where compressive total stress is applied and held as constant throughout, the effective stress is positive (compressive) everywhere in the sample. As the same viscoplastic law states, the compaction rate will become faster if there is a perturbation that causes the effective stress to be larger, which will reduce pore pressure in order to keep a constant total stress. This will in turn lead to an even larger effective stress on the solid phase and will once again reduce the pore pressure as the results of maintaining the constant total stress. This shedding process from the pore fluid to the skeleton will make the solid phase take more stress which will eventually lead to the rearrangements (translation, displacement, or even crushing) of the grains, which have been reported in the literature to be physical characteristics resulting from the formation of compaction bands (Du Bernard et al., 2002, Fossen et al., 2007, Olsson et al., 2000).

We further note that the effects of temperature are still not very clear from the current available data. This arises primarily because the impact of temperature on the system is complex, affecting numerous variables including the material sensitivity parameter m, fluid viscosity u_f, permeability k, Biot's coefficient of effective stress A, and Skempton's pore pressure coefficient B. These latter four parameters are found in both the numerator and denominator of Eq. (28), where

they may either cancel out or interact in multifaceted ways. Consequently, the exact influence of temperature on the system remains unclear so far.

The discoveries and results from the present work can be applied as a guide to several engineering processes and applications. Taking hydraulic fracturing treatments for example, at the end of each stage there is an abrupt pressure drop associated with the end of pumping. In some cases, there is immediate flowback, while in others there could be another opportunity for rapid decompression when the well is finally flowed back at the end of a multi-stage treatment at the transition to production. Our results show that such rapid depressurization at the end of pumping can induce tensile dilation bands in the well cement sheath and thus can jeopardize the well integrity. On the other hand, if rapid depressurization is translated into the reservoir and occurs in the vicinity of the hydraulic fractures, there could be a generation of secondary fractures as dilation bands with could impact fluid flow and contribute positively to production.

Another scenario that could be leading to the occurrence of dilation bands is the process of plug verification during well plug and abandonment. Currently, none of the industrial codes delineates the appropriate loading/unloading rates for the hydraulic pressure tests which are used to verify the zonal isolation functionalities of permanent cement plugs. Because the cement is low permeability and likely rate-sensitive (recall the material used in this study is wellbore cement), it is possible that the load/unload cycle of pressure used for plug verification could, somewhat ironically, be causing damage in the form of induced dilation bands. In fact, the "better" the cement is, in the sense of having lower permeability the more susceptible it will be to dilation band formation and the associated damage to its material properties. This points to a material design tradeoff, guided by Eq. (31), wherein cement plug material should be low enough permeability to ensure zonal isolation, but high enough permeability so that the risk of damage due to dilation band formation is at an acceptable level in light of the anticipated loading/unloading rates to which it will be subjected.

5. Conclusions

A theoretical framework capturing the coupling between fluid diffusion and viscoplastic solid deformation predicts that periodic regions of tensile effective stress could form as a result of rapid depressurization of a low-permeability, rate-dependent porous material. This solution for the

effective stress S' is dependent on the material rate-sensitivity exponent m and a dimensionless strain rate ζ, where the latter embodies a comparison between the viscoplastic solid deformation rate and the diffusive dissipation of pore pressure. Mathematical solutions point to power law scaling relationships between the number of tensile zones and the dimensionless strain rate, where a higher dimensionless strain rate (i.e. higher actual strain rate and/or smaller diffusivity of the porous material) results in more closely-spaced regions of tensile stress. More specifically, there are at least two distinct zones with different power laws, one for smaller values of ζ and another for larger values, with the transition occurring when this quantity is in the hundreds.

As a proof of concept to the dilation bands predicted by theory, their emergence is observed in experiments on fully-saturated cylindrical cement samples during the decompression tests with different releasing speeds. The experimental observations show that a faster unloading time will cause a higher number of (i.e. a smaller spacing between) the periodic tensile fractures. The exponent of the power law relationship between unloading time and dilation band spacing from the experimental observations is found to fall into ranges consistent with theoretical predictions.

Based on this initial level of consistency between theory and experiment, the observed formation of the periodic dilation bands is inferred to occur when the strain rate is following a viscoplastic law and fluid flow is following Darcy's law. To satisfy mass balance, solid deformation must induce a counterflow of fluid. At the same time, whenever fluid pressure increases, it takes more of the load and so to maintain constant total stress, more load must be shifted away from the skeleton, thereby further decreasing the effective stress (making it more tensile). This positive feedback is proposed to be the underlying mechanism of dilation band formation that leads to the observation of planar opening-mode fractures with two discrete and neat surfaces in the low permeable porous materials with strong rate dependency.

The mechanism of dilation band formation could be responsible for periodic tensile fracturing in a variety of low-permeability, rate dependent porous materials such as wellbore cement and clay-rich rocks. Focusing on engineering timescales this work shows both the potential pitfalls of dilation band formation that could lead to the reduction of zonal isolation provided by wellbore cement as well as possible benefits if dilation bands form near hydraulic fractures in reservoir rocks and increase the ability of oil and gas to flow to a well. The coupling that leads to these behaviors furthermore comprises a new way to see porous materials, even at an intuitive

552 level, as being prone to localization of dilation in a manner that is spontaneous and regular in its
553 behavior.

554

555 Acknowledgments

556 This research was supported by the National Academy of Science and Mathematics Gulf Research
557 Program (NASEM-GRP) grant # 10002358 and the Project Research Team Members: Mileva
558 Radonjic and her group from Oklahoma State University, Raissa Ferron and her group from
559 University of Texas Austin, Ipsita Gupta and her group from Louisiana State University, and Pierre
560 Cerasi and his team from SINTEF. Thanks go to Charles Hager (PITT) for the outstanding
561 technical contributions and Aubrey Green (PITT) for the helpful grammatical edits.

562

563 References:

564 Abramowitz, M., & Stegun, I. A. (1964). *Handbook of mathematical functions with formulas,*
565 *graphs, and mathematical tables* (Vol. 55): US Government printing office.
566 Agofack, N., Ghabezloo, S., Sulem, J., Garnier, A., & Urbanczyk, C. (2019). Experimental
567 investigation of the early-age mechanical behaviour of oil-well cement paste. *Cement and*
568 *Concrete Research, 117*, 91-102.
569 Antonellini, M., & Aydin, A. (1994). Effect of faulting on fluid flow in porous sandstones:
570 petrophysical properties. *AAPG bulletin, 78*(3), 355-377.
571 Antonellini, M., & Aydin, A. (1995). Effect of faulting on fluid flow in porous sandstones:
572 geometry and spatial distribution. *AAPG bulletin, 79*(5), 642-671.
573 Banthia, N., & Mindess, S. (1989). Water permeability of cement paste. *Cement and Concrete*
574 *Research, 19*(5), 727-736.
575 Baud, P., Klein, E., & Wong, T.-f. (2004). Compaction localization in porous sandstones: spatial
576 evolution of damage and acoustic emission activity. *Journal of Structural Geology, 26*(4),
577 603-624.
578 Bésuelle, P. (2001). Evolution of strain localisation with stress in a sandstone: brittle and semi-
579 brittle regimes. *Physics and Chemistry of the Earth, Part A: Solid Earth and Geodesy,*
580 *26*(1-2), 101-106.
581 Biot, M. A. (1941). General theory of three-dimensional consolidation. *Journal of applied*
582 *physics, 12*(2), 155-164.
583 Borja, R., & Kavazanjian, E. (1985). A constitutive model for the stress–strain–time behaviour
584 of 'wet'clays. *Geotechnique, 35*(3), 283-298.
585 Borja, R. I. (2004). Computational modeling of deformation bands in granular media. II.
586 Numerical simulations. *Computer Methods in Applied Mechanics and Engineering,*
587 *193*(27-29), 2699-2718.

588 Cheng, A. H.-D. (1993). Fundamentals of poroelasticity. In *Analysis and design methods* (pp.
589 113-171): Elsevier.
590 Detournay, E., & Atkinson, C. (2000). Influence of pore pressure on the drilling response in low-
591 permeability shear-dilatant rocks. *International Journal of Rock Mechanics and Mining*
592 *Sciences, 37*(7), 1091-1101.
593 Detournay, E., & Cheng, A.-D. (1988). *Poroelastic response of a borehole in a non-hydrostatic*
594 *stress field.* Paper presented at the International Journal of Rock Mechanics and Mining
595 Sciences & Geomechanics Abstracts.
596 Du Bernard, X., Eichhubl, P., & Aydin, A. (2002). Dilation bands: A new form of localized
597 failure in granular media. *Geophysical Research Letters, 29*(24), 29-21-29-24.
598 Eichhubl, P., Hooker, J. N., & Laubach, S. E. (2010). Pure and shear-enhanced compaction
599 bands in Aztec Sandstone. *Journal of Structural Geology, 32*(12), 1873-1886.
600 Fossen, H., Schultz, R. A., Shipton, Z. K., & Mair, K. (2007). Deformation bands in sandstone: a
601 review. *Journal of the Geological Society, 164*(4), 755-769.
602 Gapais, D. (1989). Shear structures within deformed granites: mechanical and thermal indicators.
603 *Geology, 17*(12), 1144-1147.
604 Gersevanov, N. (1937). Fundamentals of soil masses dynamics. *StroyIzdat, Moscow*.
605 Ghabezloo, S. (2010). Association of macroscopic laboratory testing and micromechanics
606 modelling for the evaluation of the poroelastic parameters of a hardened cement paste.
607 *Cement and Concrete Research, 40*(8), 1197-1210.
608 Ghabezloo, S., Sulem, J., Guédon, S., Martineau, F., & Saint-Marc, J. (2008). Poromechanical
609 behaviour of hardened cement paste under isotropic loading. *Cement and Concrete*
610 *Research, 38*(12), 1424-1437.
611 Goto, S., & Roy, D. M. (1981). The effect of w/c ratio and curing temperature on the
612 permeability of hardened cement paste. *Cement and Concrete Research, 11*(4), 575-579.
613 Hickman, R., & Gutierrez, M. (2007). Formulation of a three-dimensional rate-dependent
614 constitutive model for chalk and porous rocks. *International journal for numerical and*
615 *analytical methods in geomechanics, 31*(4), 583-605.
616 Issen, K. A., & Rudnicki, J. W. (2000). Conditions for compaction bands in porous rock. *Journal*
617 *of Geophysical Research: Solid Earth, 105*(B9), 21529-21536.
618 Jackson, M. P., & Talbot, C. J. (1986). External shapes, strain rates, and dynamics of salt
619 structures. *Geological Society of America Bulletin, 97*(3), 305-323.
620 Jacquey, A. B., Rattez, H., & Veveakis, M. (2021). Strain localization regularization and patterns
621 formation in rate-dependent plastic materials with multiphysics coupling. *Journal of the*
622 *Mechanics and Physics of Solids, 152*, 104422.
623 Jamison, W. R., & Stearns, D. W. (1982). Tectonic deformation of Wingate Sandstone, Colorado
624 National Monument. *AAPG bulletin, 66*(12), 2584-2608.
625 Katende, A., Lu, Y., Bunger, A., & Radonjic, M. (2020). Experimental quantification of the
626 effect of oil based drilling fluid contamination on properties of wellbore cement. *Journal*
627 *of Natural Gas Science and Engineering, 79*, 103328.
628 Khalifeh, M., & Saasen, A. (2020). *Introduction to permanent plug and abandonment of wells*:
629 Springer Nature.
630 Li, Y., & Li, J. (2015). Relationship between fracture area and tensile strength of cement paste
631 with supplementary cementitious materials. *Construction and Building Materials, 79*,
632 223-228.

633 Lu, Y., & Bunger, A. Semi-Analytical Solution for Thermo-Poro-Elastic Stresses in a Wellbore
634 Cement Plug and Implications for Cement Properties that Minimize Risk of Failure.
635 Nyame, B., & Illston, J. (1981). Relationships between permeability and pore structure of
636 hardened cement paste. *Magazine of Concrete Research, 33*(116), 139-146.
637 Okubo, C. H., & Schultz, R. A. (2005). Evolution of damage zone geometry and intensity in
638 porous sandstone: insight gained from strain energy density. *Journal of the Geological*
639 *Society, 162*(6), 939-949.
640 Olsson, W., & Holcomb, D. (2000). Compaction localization in porous rock. *Geophysical*
641 *Research Letters, 27*(21), 3537-3540.
642 Olsson, W. A. (1999). Theoretical and experimental investigation of compaction bands in porous
643 rock. *Journal of Geophysical Research: Solid Earth, 104*(B4), 7219-7228.
644 Olsson, W. A., Lorenz, J. C., & Cooper, S. P. (2004). A mechanical model for multiply-oriented
645 conjugate deformation bands. *Journal of Structural Geology, 26*(2), 325-338.
646 Pearson, C. (1981). The relationship between microseismicity and high pore pressures during
647 hydraulic stimulation experiments in low permeability granitic rocks. *Journal of*
648 *Geophysical Research: Solid Earth, 86*(B9), 7855-7864.
649 Pfiffner, O.-A., & Ramsay, J. (1982). Constraints on geological strain rates: arguments from
650 finite strain states of naturally deformed rocks. *Journal of Geophysical Research: Solid*
651 *Earth, 87*(B1), 311-321.
652 Pittman, E. D. (1981). Effect of fault-related granulation on porosity and permeability of quartz
653 sandstones, Simpson Group (Ordovician), Oklahoma. *AAPG bulletin, 65*(11), 2381-2387.
654 Regenauer-Lieb, K., Veveakis, M., Poulet, T., Wellmann, F., Karrech, A., Liu, J., Hauser, J.,
655 Schrank, C., Gaede, O., & Fusseis, F. (2013). Multiscale coupling and multiphysics
656 approaches in earth sciences: Applications. *Journal of Coupled Systems and Multiscale*
657 *Dynamics, 1*(3), 281-323.
658 Rudnicki, J. W., & Rice, J. (1975). Conditions for the localization of deformation in pressure-
659 sensitive dilatant materials. *Journal of the Mechanics and Physics of Solids, 23*(6), 371-
660 394.
661 Schmitt, D., & Zoback, M. (1989). *Laboratory tests of the effects of pore pressure on tensile*
662 *failure.* Paper presented at the ISRM International Symposium, paper number: ISRM-IS-
663 1989-111.
664 Sigda, J. M., Goodwin, L. B., Mozley, P. S., & Wilson, J. L. (1999). Permeability alteration in
665 small-displacement faults in poorly lithified sediments: Rio Grande Rift, Central New
666 Mexico. *Washington DC American Geophysical Union Geophysical Monograph Series,*
667 *113*, 51-68.
668 Tamtsia, B. T., & Beaudoin, J. J. (2000). Basic creep of hardened cement paste A re-examination
669 of the role of water. *Cement and Concrete Research, 30*(9), 1465-1475.
670 Taylor, D. W. (1948). *Fundamentals of soil mechanics* (Vol. 66): LWW.
671 Terzaghi, K. (1925). *Erdbaumechanik auf bodenphysikalischer Grundlage*: F. Deuticke.
672 Veveakis, E., Alevizos, S., & Vardoulakis, I. (2010). Chemical reaction capping of thermal
673 instabilities during shear of frictional faults. *Journal of the Mechanics and Physics of*
674 *Solids, 58*(9), 1175-1194.
675 Veveakis, E., & Regenauer-Lieb, K. (2015). Cnoidal waves in solids. *Journal of the Mechanics*
676 *and Physics of Solids, 78*, 231-248.
677 Wolf, H., König, D., & Triantafyllidis, T. (2003). Experimental investigation of shear band
678 patterns in granular material. *Journal of Structural Geology, 25*(8), 1229-1240.

679 Wong, T. f., Baud, P., & Klein, E. (2001). Localized failure modes in a compactant porous rock.
680 *Geophysical Research Letters, 28*(13), 2521-2524.
681 Wyrzykowski, M., Scrivener, K., & Lura, P. (2019). Basic creep of cement paste at early age-the
682 role of cement hydration. *Cement and Concrete Research, 116*, 191-201.

683